JGR Space Physics

RESEARCH ARTICLE
10.1029/2019JA027545

Key Point:
- The diffusive equilibrium density model provides a global map of a two-species plasma distribution in Saturn's inner magnetosphere

Supporting Information:
- Supporting Information S1

Correspondence to:
A. M. Persoon,
ann-persoon@uiowa.edu

Citation:
Persoon, A. M., Kurth, W. S., Gurnett, D. A., Faden, J. B., Groene, J. B., Morooka, M. W., et al. (2020). The plasma distribution in Saturn's inner magnetosphere from 2.4 to 10 R_S: A diffusive equilibrium model. *Journal of Geophysical Research: Space Physics*, *125*, e2019JA027545. https://doi.org/10.1029/2019JA027545

Received 15 OCT 2019
Accepted 6 FEB 2020
Accepted article online 9 MAR 2020

Distribution in Saturn's Inner Magnetosphere From 2.4 to 10 R_S: A Diffusive Equilibrium Model

A. M. Persoon[1], W. S. Kurth[1], D. A. Gurnett[1], J. B. Faden[1], J. B. Groene[1], M. W. Morooka[2], J. E. Wahlund[2], R. J. Wilson[3], and J. D. Menietti[1]

[1]Department of Physics and Astronomy, University of Iowa, Iowa City, IA, USA, [2]Swedish Institute of Physics, Uppsala, Sweden, [3]Laboratory for Atmospheric and Space Physics, University of Colorado, Boulder, CO, USA

Abstract Electron density measurements have been obtained by the Cassini Radio and Plasma Wave Science (RPWS) instrument covering the period from 30 June 2004 to 19 April 2017, spanning latitudes up to ~30° and *L* values from 2.4 to 10. Near the F ring, electron densities are derived from RPWS measurements of electron plasma oscillations at high latitudes and from the Langmuir Probe (RPWS/LP) sweep data at low latitudes. The electron density measurements from the ring-grazing orbits, beginning in December 2016, have made it possible to extend the work of a previous diffusive equilibrium model to include the distribution of the ring plasma. Beyond the ring-grazing orbits, the densities are derived from RPWS measurements of the upper hybrid resonance frequency. These density measurements are used to anchor the fit of an expanded diffusive equilibrium density model for a two-species plasma consisting of water group and hydrogen ions in Saturn's inner magnetosphere. Density contour plots for the two ion species and the electrons are presented. The distribution of the derived plasma densities is consistent with two primary sources, the Enceladus plume and the extended ring atmosphere. There is also an indication of a weaker plasma source at Dione. In the region just outside the A ring and in the region including the Enceladus orbit, the diffusive equilibrium model also shows the expansion of lighter ions and electrons to higher latitudes along the magnetic field lines with evidence of a weaker plasma expansion between the orbits of Tethys and Dione.

1. Introduction

Between 1979 and 1981, the Pioneer 11, Voyager 1, and Voyager 2 spacecraft each flew by Saturn and obtained the first measurements of the planet's magnetospheric plasma (Bridge et al., 1981, 1982; Eviatar et al., 1983; Frank et al., 1980; Lazarus & McNutt, 1983; Maurice et al., 1996; Richardson, 1986; Sittler et al., 1983; Trainor et al., 1980; Wolfe et al., 1980). Thermal plasma density measurements from the two Voyager flybys were used to constrain a diffusive transport model for the plasma using the force balance equation (see equation 1 below) to track the plasma along a magnetic field line (Richardson, 1995; Richardson, 1998; Richardson & Sittler, 1990). Different models for the distribution of water group neutrals (Jurac et al., 2002; Richardson, 1998; Richardson et al., 1998) were combined with the diffusive plasma transport model, and the resulting neutral and plasma density equations were solved iteratively to develop a self-consistent density model based on neutral-plasma chemistry, resulting in density contour maps of the neutrals and magnetospheric plasma components (Jurac & Richardson, 2005; Richardson, 1998; Richardson et al., 1998; Richardson & Jurac, 2004).

On 30 June 2004, Cassini arrived at Saturn to begin a series of more than 290 orbits through Saturn's magnetosphere that would last more than 13 years. Among the fleet of instruments onboard the Cassini orbiter that would provide in situ measurements in Saturn's inner magnetosphere were two instruments that would measure thermal plasma parameters, plasma waves and dust particles. The Cassini Plasma Spectrometer (CAPS) investigation provided measurements of plasma composition, and plasma parameters derived from moments of the charged particle distributions (Coates et al., 2005; Young et al., 2004, 2005). The Cassini Radio and Plasma Wave Science (RPWS) investigation, including a Langmuir probe, measured electric and magnetic fields over a wide range of frequencies to study radio emissions, dust impacts, and plasma waves and to derive thermal plasma parameters (Gurnett et al., 2004, 2005; Wahlund et al., 2005). Density measurements from these instruments were used to derive density models from power-law fits to the data measurements that illustrated the radial distribution of the equatorial plasma in the inner magnetosphere

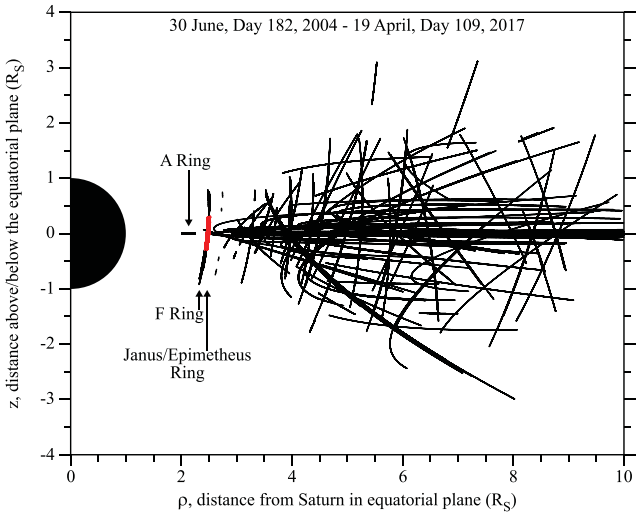

Figure 1. A meridional plot showing the distribution of the RPWS electron density measurements from Saturn Orbit Insertion (SOI) on 30 June 2004 until the end of the ring-grazing orbits on 19 April 2017. Densities near the Janus/Epimetheus ring, measured by the Langmuir Probe instrument (RPWS/LP), are shown in red. The distribution of the density measurements is plotted in the (ρ, z) plane where ρ is the distance from Saturn's spin axis and z is the distance above/below Saturn's equatorial plane.

for ions (Thomsen et al., 2010; Wilson et al., 2008, 2017) and electrons (Morooka et al., 2009; Persoon et al., 2005, 2013; Schippers et al., 2008, 2013). Density measurements at higher latitudes led to density models with exponential scale heights that illustrated the gradual roll-off in the density with increasing latitude for the electrons (Morooka et al., 2009; Persoon et al., 2006) and the ions (Thomsen et al., 2010; Wilson et al., 2008).

When sufficient density measurements became available at higher latitudes, more complex plasma density models were developed for a two-species plasma. Using the field-aligned force balance equations from Maurice et al. (1997) and CAPS ion and electron input parameters, Sittler et al. (2008) self-consistently solved for the ion distribution along magnetic field lines and created contour plots of the heavy water group ions, the light hydrogen ions, and the electrons out to 10 Saturn radii (R_S). Persoon et al. (2009) used RPWS electron density measurements and plasma input parameters from CAPS and RPWS to develop a diffusive equilibrium density model for a two-species plasma, derived from the magnetic field-aligned force equation of Richardson and Sittler (1990). A series of coordinate transformations, substitutions, and assumptions resulted in a simplified analytical model that, like the Sittler et al. (2008) model, produced a series of contour plots to describe the distribution of the heavy water group ions, the light hydrogen ions, and the electrons out to 10 R_S. These two-species plasma distribution models for Saturn's inner magnetosphere focused on the inner magnetospheric plasma that has Enceladus as the primary source. The objective of this study is to extend the diffusive equilibrium model of Persoon et al. (2009) inward to include the distribution of plasma that is generated through photoionization in the extended ring atmosphere just beyond the outer boundary of the A ring (Gurnett et al., 2005; Persoon et al., 2015).

By 23 April 2017, Cassini had completed 272 orbits through Saturn's inner magnetosphere beyond the main ring system. Cassini's RPWS instrument had obtained more than 661,000 electron density measurements. The data range from L-shells of 2.4 to 10 and extend up to ~30° in latitude, providing sufficient latitudinal coverage to resolve the light ion component of the magnetospheric plasma. Figure 1 is a meridional plot showing the spatial distribution of the RPWS electron density measurements from Saturn Orbit Insertion (SOI) on 30 June to 1 July 2004 to the last measurements of the ring-grazing orbits obtained on 19 April 2017. The black lines indicate electron densities derived from the upper hybrid resonance emissions (Persoon et al., 2005) and the electron plasma oscillations (see discussion in section 8 below). The red lines indicate electron densities derived by the Langmuir Probe (RPWS/LP) instrument (see discussion in section 8 below). The electron densities obtained during the ring-grazing orbits, along with the densities obtained near the outer boundary of the A ring during orbit insertion in 2004, make it possible to extend the diffusive equilibrium model inward to $L = 2.4$ to include the ring plasma. These density measurements will constrain the fit of the diffusive equilibrium density model for a two-species plasma in Saturn's inner magnetosphere out to $L = 10$.

2. RPWS Measurements of the Electron Density in the Inner Magnetosphere

2.1. The Ring Plasma: Electron Density Measurements

When Cassini arrived at Saturn on 30 June 2004, RPWS found evidence of severely depleted electron densities over the main rings and an electron density peak, several orders of magnitude greater than the densities measured over the rings, in the region beyond the outer edge of the A ring (Gurnett et al., 2005). The enhanced electron densities in this region are the result of photodissociated water group neutrals from the ring atmosphere that have been scattered into the extended ring atmosphere beyond the outer boundary of the A ring and subsequently photoionized (Ip, 2005; Johnson et al., 2006; Persoon et al., 2015).

Cassini would not return to the region just beyond the A ring again until the ring-grazing orbits began in November 2016. The ring-grazing orbits were a series of 20 highly inclined orbits (30 November 2016

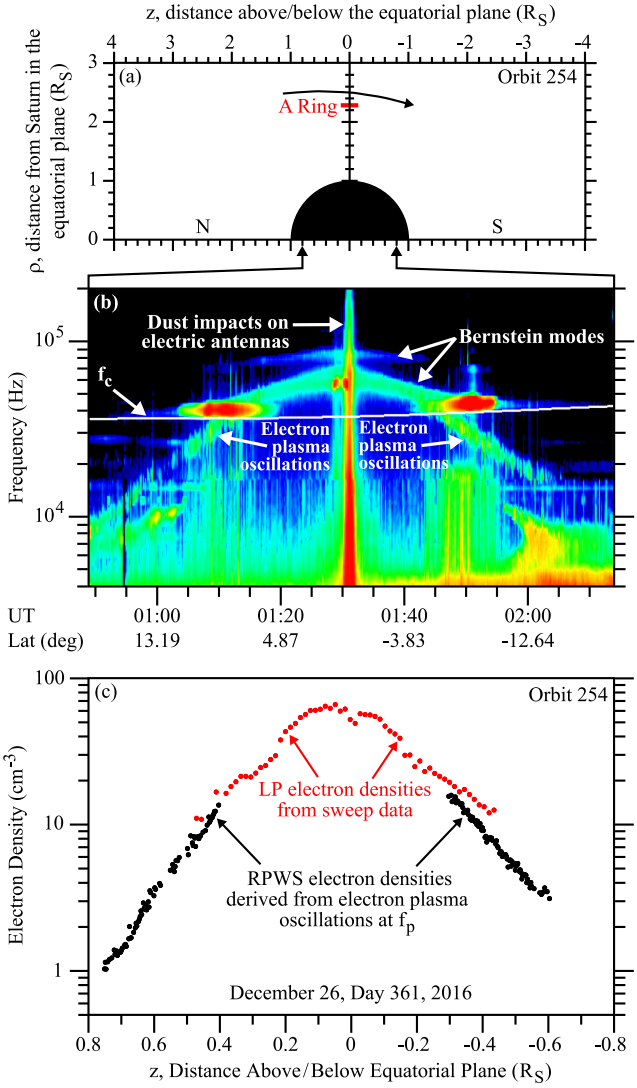

Figure 2. RPWS observations near the Janus/Epimetheus ring during orbit 254 on 26 December 2016. The high-inclination of the spacecraft trajectory from north to south (left to right) is shown in panel a. Panel b is an electric field spectrogram for the 00:45–02:15 UT time interval showing the electron plasma oscillations that occur at higher latitudes before and after the ring plane crossing at 01:31 UT. Panel c is an electron density profile plot of the RPWS high-latitude electron densities (in black), derived from the electron plasma oscillations for the same 90-minute time interval, and the RPWS/LP low-latitude electron densities (in red) derived using the Langmuir probe sweep method.

through 22 April 2017) that passed from north to south through the ring plane between 2.46 and 2.52 R_S near periapsis. For these orbits, RPWS obtained electron density measurements from electron plasma oscillations at the electron plasma frequency (f_p). The electron density (n_e) is derived from the electron plasma frequency using the simple equation $f_p = 9\sqrt{n_e}$ where f_p is given in kilohertz and n_e is in particles per cubic centimeter. Figure 2a shows the high-inclination, north to south (left to right) spacecraft trajectory for the 90-min time interval centered on the ring plane crossing at 01:31 UT on 26 December 2016. Cassini passes through the ring plane beyond the outer edge of the A ring, located at 2.27 R_S. Figure 2b is an electric field spectrogram for the same 90-min period. The electron plasma oscillations can be found at the higher latitudes before and after the ring plane crossing. At low latitudes near the ring plane, strong Bernstein modes and very intense dust impacts on the electric antennas (Ye et al., 2014) obscure the much weaker upper hybrid emissions making it impossible to derive the electron density near the equatorial plane.

In the high-density regions, we use electron density measurements derived from the Langmuir Probe (RPWS/LP) sweeps (Gustafsson & Wahlund, 2010; Morooka et al., 2011). Because the sweep method is not sensitive to low densities, only measurements ≥10 cm^{-3} have been used. This constraint removes most, but not all, of the LP density measurements in the low density regions at higher latitudes where the LP and RPWS density measurements diverge. The LP measurements provide all of the low-latitude densities, and the f_p measurements from the electron plasma oscillations provide the high-latitude densities that will anchor the fit for the diffusive equilibrium model in this innermost region of the magnetosphere (see section 5). Figure 2c is a plot of the electron densities derived from the RPWS measurements of the electron plasma oscillations in panel b and the RPWS/LP density measurements derived from the sweep method. For this highly inclined orbit, the electron densities peak at ~70 cm^{-3} just north of the equatorial plane (Morooka et al., 2018). Because the ring-grazing orbits are nearly perpendicular to the equatorial plane at periapsis (see Figure 1), the densities are plotted along the z axis, parallel to Saturn's spin axis, in the equatorial coordinate system. The average uncertainty in the RPWS electron density measurements for orbit 254 is 15%. The average uncertainty in the RPWS/LP electron density measurements for orbit 254 is 10%.

Figure 3 shows the north-to-south distribution of all of the nearly 1800 electron density measurements from the ring-grazing orbits. The LP electron densities (in red) show the expected strong density peak near the equatorial plane (Morooka et al., 2018). A few LP density measurements at higher latitudes have survived the ≥10-cm^{-3} constraint on LP density measurements derived from the sweep method. In the binning and averaging process used in this study, these LP measurements are combined and averaged with the RPWS densities. All of the RPWS electron density data used in this study are available in the Planetary Data System. These archived data files contain normalized density errors for each measurement. The average uncertainty in the RPWS electron density measurements in Figure 3 is 15%. The LP density data have an average density uncertainty of 10%. A more detailed discussion of the error analysis in the LP data is contained in Morooka et al. (2019).

The electron density measurements in Figure 3 show a consistent density roll-off with increasing distance from the equatorial plane and a strong orbit-to-orbit variability at all latitudes, with the largest variation evident at the lowest latitudes. Morooka et al. (2018) attribute the highly variable electron densities measured

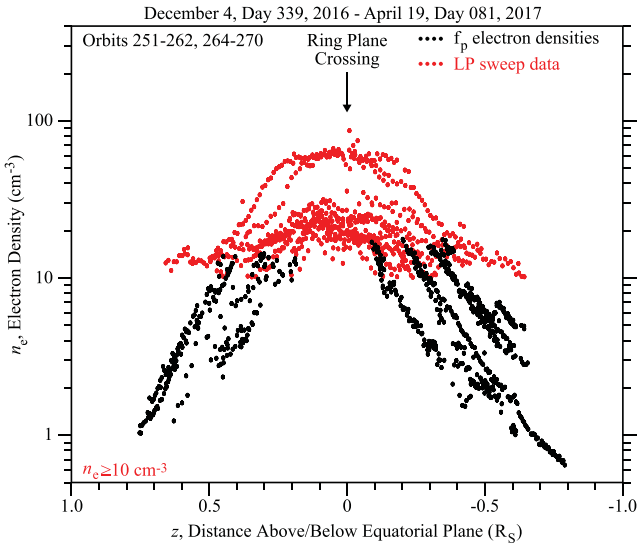

Figure 3. The north-south distribution of the RPWS electron density measurements (in black) and the RPWS/LP electron density measurements (in red) for all of the ring-grazing orbits. The densities are plotted along the z axis, parallel to Saturn's spin axis.

during the ring-grazing orbits to changes in the size and distribution of the dust particles in this equatorial region that contains the dusty Janus/Epimetheus and F rings. Dust grains in the Enceladus plume region had been previously associated with the absorption of thermal electrons (Farrell et al., 2009; Morooka et al., 2011) and have now been shown to affect the distribution of electrons near the faint and dusty inner rings just outside the main ring system (Johnson et al., 2017; Morooka et al., 2018).

2.2. The Enceladus Plasma: Electron Density Measurements

With the exception of the ring-grazing orbits, all of the RPWS electron densities used in this study were derived from the upper hybrid resonance emissions which peak at the upper hybrid resonance frequency, $f_{UH} = \sqrt{f_c^2 + f_p^2}$, where f_c is the electron cyclotron frequency and $f_p = 9\sqrt{n_e}$ is the electron plasma frequency (in kilohertz) as a function of the electron density n_e in particles per cubic centimeter. The upper hybrid resonance emissions are visible on nearly every Cassini orbit out to $L = 10$ and up to latitudes of ~30°. Unlike the ring plasma, which is subject to seasonal variations (Elrod et al., 2014; Persoon et al., 2015) and strong dust absorption effects (Morooka et al., 2018; Ye et al., 2014), the Enceladus plasma, especially outside 5 R_S, shows much less variability from orbit to orbit (Persoon et al., 2005, 2013, 2015). Orbit-to-orbit variations in the plasma distribution due to strong dust absorption effects are a significant factor in the vicinity of the plume. However, there are few RPWS density measurements in the plume region due to the dust impacts on the electric antennas, which obscure the upper hybrid resonance emissions (Ye et al., 2014).

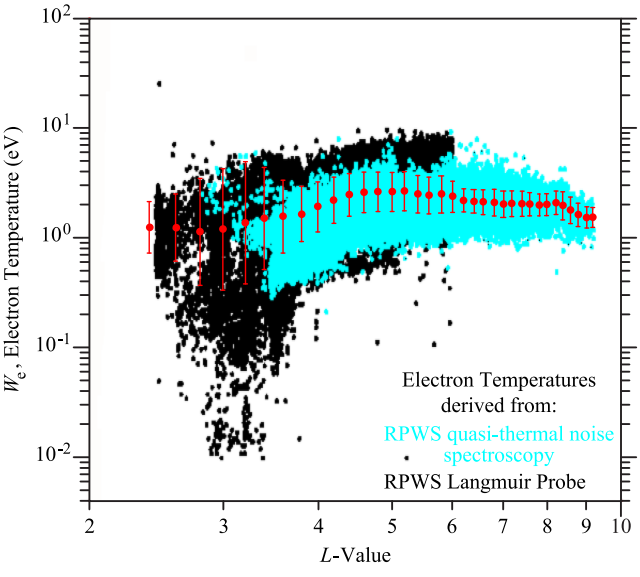

Figure 4. A plot of the RPWS electron temperatures obtained from the quasi-thermal noise spectroscopy (QTN) method (in blue) and the RPWS/LP sweep method (in black) as a function of L-shell. The temperature measurements have been averaged in L-shell bins of 0.4 R_S (red circles) and smoothed with a sliding average of 0.2 R_S. The error bars represent one standard deviation of the averaged temperatures.

3. The Diffusive Equilibrium Model

The terms in the magnetic field-aligned force equation describe the forces acting on a charged particle constrained to move along a magnetic field line in a rapidly corotating magnetosphere (Richardson & Sittler, 1990):

$$\frac{\partial P_{\|i}}{\partial s} = \left(P_{\|i} - P_{\perp i}\right)\frac{1}{B}\frac{\partial B}{\partial s} + n_i m_i \frac{\partial}{\partial s}\left(\frac{1}{2}\Omega^2\rho^2\right) + n_i \frac{\partial}{\partial s}\left(\frac{GM_S m_i}{r}\right) - n_i q_i \frac{\partial \Phi}{\partial s}. \quad (1)$$

The term on the left side of this equation is the parallel pressure gradient force where s is the distance along the field line and $P_{\|}$ is the parallel pressure. The terms on the right side of the equation represent the magnetic mirror force, the centrifugal force, the gravitational force, and the ambipolar force, respectively, where $P_{\perp}$ is the perpendicular pressure, B is the magnetic field strength, n_i and m_i are the particle density and mass, Ω is the plasma rotation rate, ρ is the distance from Saturn's spin axis, G is the gravitational constant, M_S is the mass of Saturn, r is the radial distance from the center of Saturn, q_i is the particle charge, and Φ is the electrostatic potential. Saturn's corotating magnetosphere results in a strong centrifugal force that dominates over the planet's gravitational pull on all charged particles beyond the synchronous point at 1.86 R_S.

The equations for the density of the heavy water group ions (W^+), the light hydrogen ions (H^+), and the electrons are derived from equation 1, assuming charge neutrality:

Table 1
Plasma Parameters Used in the Model

L-shell	Electron temperatures (eV)	W^+ ion anisotropies	H^+ ion anisotropies
2.4	1.245	3.0	1.5
2.6	1.238	3.0	1.5
2.8	1.132	3.0	1.5
3.0	1.191	3.0	1.5
3.2	1.369	3.0	1.5
3.4	1.498	3.0	1.5
3.6	1.557	3.0	1.5
3.8	1.639	3.0	1.5
4.0	1.913	3.0	1.5
4.2	2.199	2.973	1.517
4.4	2.462	2.980	1.493
4.6	2.594	3.082	1.660
4.8	2.624	3.123	1.756
5.0	2.634	2.980	1.642
5.2	2.657	2.838	1.528
5.4	2.511	2.646	1.461
5.6	2.429	2.437	1.410
5.8	2.484	2.285	1.390
6.0	2.365	2.303	1.462
6.2	2.193	2.320	1.534
6.4	2.152	2.263	1.569
6.6	2.112	2.182	1.590
6.8	2.091	2.079	1.616
7.0	2.024	1.908	1.653
7.2	2.043	1.736	1.691
7.4	2.044	1.698	1.675
7.6	2.021	1.705	1.642
7.8	1.996	1.694	1.625
8.0	2.004	1.635	1.658
8.2	2.086	1.575	1.691
8.4	1.957	1.545	1.698
8.6	1.779	1.524	1.696
8.8	1.617	1.510	1.706
9.0	1.534	1.515	1.751
9.2	1.533	1.521	1.796
9.4	1.5	1.481	1.802
9.6	1.5	1.426	1.795
9.8	1.5	1.366	1.783
10.0	1.5	1.293	1.758

$$n_{W^+} = n_{eqW^+}\exp\left[-A_{W^+} + \ln\left[\frac{1}{\cos^6\lambda}\left(1+3\sin^2\lambda\right)^{1/2}\right] - \frac{1}{3}\frac{L^2}{H_{W^+}^2}\left(1-\cos^6\lambda\right) + \frac{\alpha}{L}\frac{\tan^2\lambda}{H_{W^+}^2} - \frac{\beta_{W^+}}{H_{W^+}^2}\Phi\right], \quad (2)$$

$$n_{H^+} = n_{eqH^+}\exp\left[-A_{H^+} + \ln\left[\frac{1}{\cos^6\lambda}\left(1+3\sin^2\lambda\right)^{1/2}\right] - \frac{1}{3}\frac{L^2}{H_{H^+}^2}\left(1-\cos^6\lambda\right) + \frac{\alpha}{L}\frac{\tan^2\lambda}{H_{H^+}^2} - \frac{\beta_{H^+}}{H_{H^+}^2}\Phi\right], \quad (3)$$

$$n_e = \left[n_{eqW^+} + n_{eqH^+}\right]\exp\left[\frac{\Phi}{W_e}\right]. \quad (4)$$

In these equations, L and λ refer to L-shell and latitude. α, β_{W^+}, and β_{H^+} are constants used to simplify the gravitation and ambipolar terms and are defined in the Appendix of Persoon et al. (2009). The isotropic electron temperature W_e and the ion temperature anisotropies, $A_i = (T_\perp/T_\parallel)_i$, are provided by the CAPS and RPWS instruments (see discussion in the following section) as inputs to the diffusive equilibrium model. The best fit of the diffusive equilibrium model to the electron density measurements gives the ion equatorial densities, n_{eqW^+} and n_{eqH^+}, and the ion scale heights, H_{W^+} and H_{H^+}. The electrostatic potential Φ is

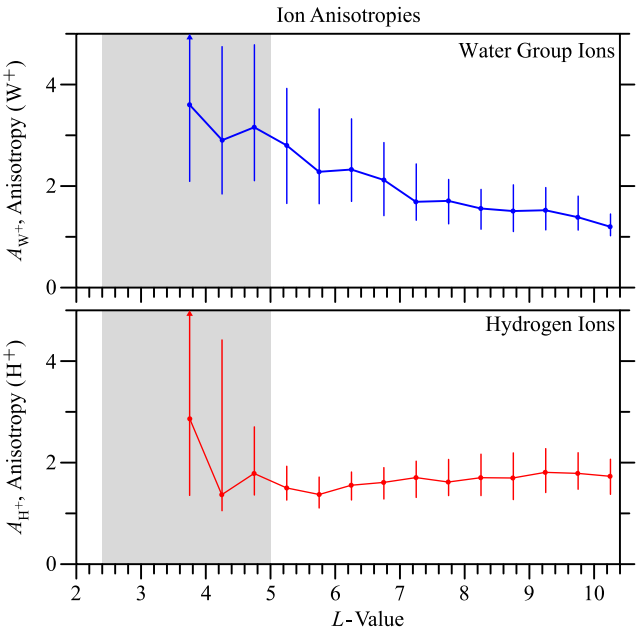

Figure 5. A plot of the CAPS ion anisotropies for the water group ions (in blue) and the hydrogen ions (in red). The median anisotropy values are plotted in 0.5 R_S bins from 3.75 to 10.25 R_S. The error bars illustrate the range between the 25% and 75% quartiles (see the Supporting Information).

numerically solved at each point along the integration path, the magnetic field line, using the charge neutrality condition, $n_e = n_{W^+} + n_{H^+}$, and equation 4. The density is solved for each charged particle species along the magnetic field lines, and density contour maps will be presented to show the distribution of each species in Saturn's inner magnetosphere. The full derivation of equations 2–4 can be found in the Appendix of Persoon et al. (2009).

4. Inputs to the Model: Electron Temperature and Ion Anisotropies

In the diffusive equilibrium model, eight L-dependent parameters control the electron density: the ion equatorial densities, the ion scale heights, the electrostatic potentials, the electron temperature, and the ion anisotropies. The electron temperature and the ion anisotropies are directly measured by the RPWS and CAPS instruments. The electron temperatures are measured by the RPWS using the quasi-thermal noise (QTN) spectroscopy method (Moncuquet et al., 2005; Schippers et al., 2013) and by the RPWS/LP instrument using the sweep method (Gustafsson & Wahlund, 2010; Wahlund et al., 2005). Figure 4 shows a plot of the electron temperatures obtained using these two methods. The QTN electron temperatures (shown in blue) are available at Planetary Data System and online (http://www.lesia.obspm.fr/kronos/data/qtn/data/). The LP electron temperatures (shown in black) are available in the Planetary Data System. Both methods show a similar L-shell dependence. The electron temperature increases out to ~$L = 5$. Beyond $L = 5$, the temperatures reach a steady plateau out to ~$L = 8$. This pattern is also evident in Schippers et al. (2013) and in Livi et al. (2014). The drop in the electron temperature beyond ~$L = 8.5$ is consistent with the temperature drop observed by Schippers et al. (2008) near the outer edge of Saturn's neutral OH cloud.

The LP and QTN temperature data have been averaged in L-shell bins of 0.4 R_S (the red circles in Figure 4) and smoothed with a sliding average in increments of 0.2 R_S. The electron temperatures are constrained only by the requirement that the number of temperature measurements in each averaging bin must exceed 25 data points. The averaging bins too sparsely populated to provide reliable results were not included in this study. The LP data have been further constrained to data derived when the electron density exceeds 10 cm^{-3}, since the sweep method can reliably derive the densities and temperatures only in the high-density region of Saturn's magnetosphere. Electron temperatures are not available beyond $L = 9.2$. For this study, we duplicate the averaged QTN electron temperature at $L = 9.2$ R_S for the higher L-shell bins. The averaged electron temperatures used in this study are listed in Table 1. In this table, the L-shell in the first column represents the center of each 0.4 R_S averaging bin.

The ion anisotropies used in this study, defined as $T_\perp/T_\parallel$, are obtained from a 3-D forward model fit to the CAPS W^+ and H^+ ion species data, assuming a Maxwellian distribution and restricting the analysis to data within 10° of the equatorial plane. The ion data were acquired over a 9-year period from the arrival of Cassini at Saturn in 2004 until 2012 when the CAPS instrument was turned off. The 3-D forward model fit is described in detail by Wilson et al. (2017). The plasma parameters of the forward model fitting for both the "good data" and the "bad data" (terms ae explained in Wilson et al., 2017) are available in Wilson et al. (2017) for an L-shell range of $5.5 \leq L \leq 30$. For this study, the anisotropies were derived from the "good data" and a median value was determined for each 0.5 R_S bin. These median values are plotted as a function of radial distance in Figure 5 and are listed in Table S2 in the supporting information for the L-shell range of this study.

Anisotropy values inside 5.5 R_S are derived using the same forward model fits to the data with a cautionary note. In the region inside 5 R_S, the presence of pickup ions (Tokar et al., 2008), associated ion cyclotron waves (Leisner et al., 2006) and penetrating background radiation, can result in elevated perpendicular temperatures and, subsequently, elevated ion anisotropies with higher uncertainties. These values should be

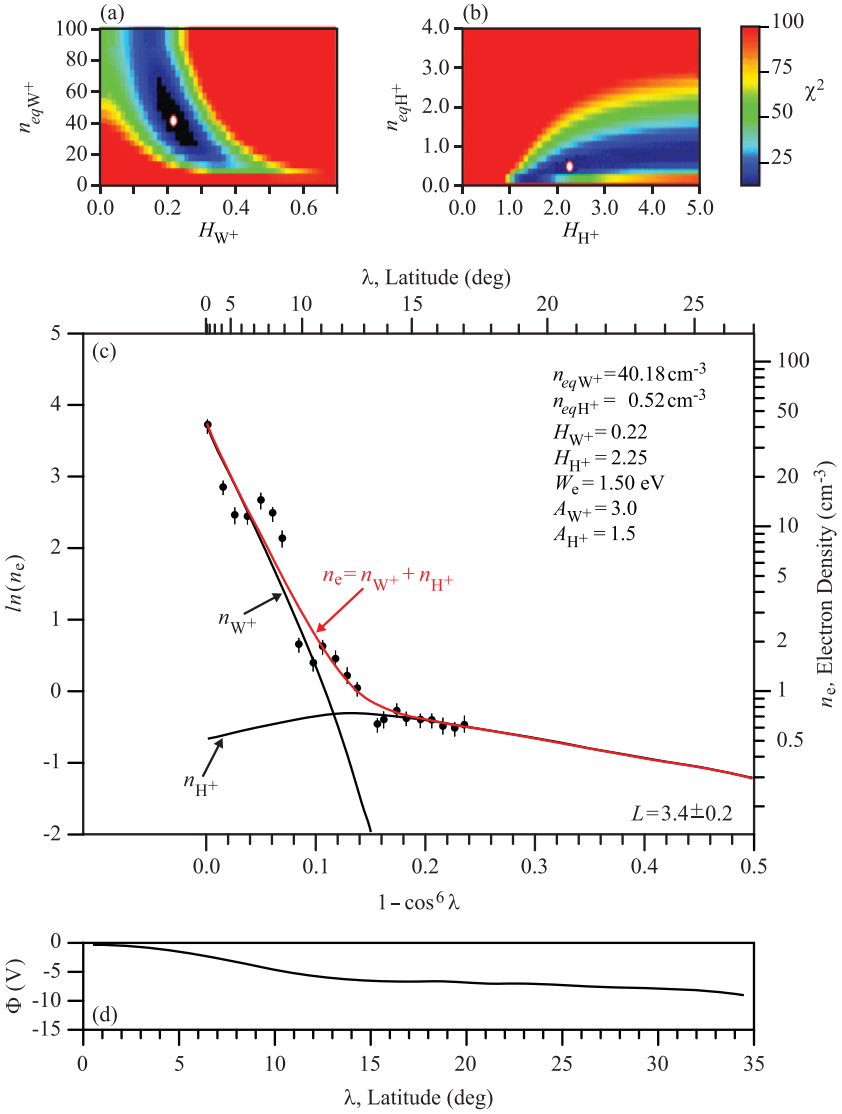

Figure 6. The diffusive equilibrium model is a best fit in four-parameter space. This figure shows the fitting process for the averaging bin centered on $L = 3.4 \pm 0.2 R_S$. Panel a shows the local minimum (white circle) in chi-square for the water group ion equatorial density (vertical scale) as a function of the scale height (horizontal scale). Panel b shows the local minimum in chi-square for the hydrogen ion equatorial density and the scale height. In both panels, there are dark regions surrounding the white circles which indicate the range of parameters that will provide the best fit of the model to the distribution of the density measurements in the $L = 3.4$ averaging bin. Panel c shows the fit of the diffusive equilibrium model to the measured electron densities, averaged over 0.4 R_S and one-degree of latitude for the $L = 3.4$ averaging bin (shown as black circles). The error bars represent one standard deviation of the averaged densities. The black lines show the solutions to the water group and hydrogen ion density equations 2 and 3. The solution for the electron density (red line) is obtained from the charge neutrality condition. Panel d is a plot of the electrostatic potentials for $L = 3.4$, which have been numerically solved at each point along the magnetic field line for $0 \leq \lambda \leq 35$ degrees.

considered as upper limits on the ion anisotropies. The ion anisotropies for the 0.2 R_S averaging bins in this study are obtained by interpolating between the median CAPS values. These anisotropies are listed in Table 1 for 39 averaging bins, where the L-shell in the first column represents the center of each 0.4 R_S averaging bin. Inside 3.75 R_S, no CAPS ion anisotropies are available.

For this study, we used two approaches to the problem of assigning ion anisotropies to the lowest L-shell bins. For the "low-anisotropy" approach, we duplicate the interpolated anisotropy value at 4.2 R_S for L-shell bins less than 4.2 R_S, avoiding the high anisotropy values with the high uncertainties at 3.8 R_S. For

Table 2
Plasma Parameters Derived from the Model

L-shell	W^+ equatorial density	H^+ equatorial density	W^+ scale height	W^+ scale height
2.4	33.48	6.55	0.11	2.95
2.6	28.60	0.40	0.33	2.85
2.8	24.67	0.60	0.42	1.60
3.0	34.42	1.86	0.16	1.85
3.2	35.70	0.46	0.17	1.52
3.4	40.18	0.52	0.22	2.25
3.6	49.68	0.55	0.37	2.10
3.8	43.17	4.83	0.29	1.10
4.0	44.67	5.11	0.39	1.34
4.2	48.95	8.54	0.34	2.08
4.4	52.40	12.01	0.34	4.72
4.6	55.30	12.90	0.37	2.97
4.8	55.91	12.97	0.43	3.22
5.0	50.71	8.11	0.57	2.57
5.2	40.03	6.42	0.79	2.60
5.4	34.65	5.65	1.02	2.20
5.6	33.55	8.59	0.79	2.78
5.8	26.86	9.14	0.75	3.18
6.0	23.51	8.27	0.84	3.13
6.2	17.79	7.77	1.05	3.42
6.4	18.34	6.47	1.14	2.41
6.6	15.80	6.02	1.33	3.81
6.8	12.77	6.85	1.24	5.03
7.0	10.54	7.49	1.02	6.17
7.2	8.27	7.53	0.82	6.89
7.4	5.99	6.60	1.07	7.03
7.6	6.46	5.52	1.17	10.00
7.8	7.20	4.45	1.03	7.72
8.0	7.61	4.07	0.96	8.10
8.2	4.85	4.22	1.15	6.64
8.4	3.66	3.86	1.44	6.12
8.6	2.90	3.66	0.86	4.28
8.8	2.45	3.10	1.21	4.15
9.0	2.26	3.39	1.10	3.35
9.2	2.08	3.04	0.95	3.59
9.4	2.37	2.62	0.99	3.95
9.6	2.06	3.15	0.73	3.34
9.8	2.15	2.26	0.91	4.03
10.0	1.73	2.21	1.10	3.21

the "high-anisotropy" approach, we duplicate the interpolated anisotropy value at 3.8 R_S for *L*-shell bins less than 3.8 R_S. The low ion anisotropy values, used in this study, are listed in Table 1. A discussion of the high anisotropy approach can be found in the supporting information.

5. Derivation of Ion Equatorial Densities and Ion Scale Heights From the Diffusive Equilibrium Model

The diffusive equilibrium model is derived from a best chi-square fit in four-parameter space $\left(n_{eqW^+}, n_{eqH^+}, H_{W^+}, \text{and } H_{H^+}\right)$. The fitting process is illustrated in Figure 6 for the averaging bin centered on $L = 3.4 \pm 0.2$ R_S. To fit the diffusive equilibrium density model to the measured RPWS electron densities, the density measurements are averaged in bins of 0.4 R_S and one-degree of latitude. Figure 6c shows the natural log of the averaged electron densities ($\ell n(n_e)$), plotted as black circles, as a function of $(1 - \cos^6\lambda)$ for the $L = 3.4$ bin. The corresponding electron densities and latitudes are shown on the right vertical axis and the top axis, respectively. The solution to the charge neutrality condition, $n_e = n_{W^+} + n_{H^+}$, is shown as a red line and represents the model fit to the measured densities. Using the right vertical axis, the black curved lines in panel c represent the density solutions to equation 2 for the water group ions and equation 3 for the

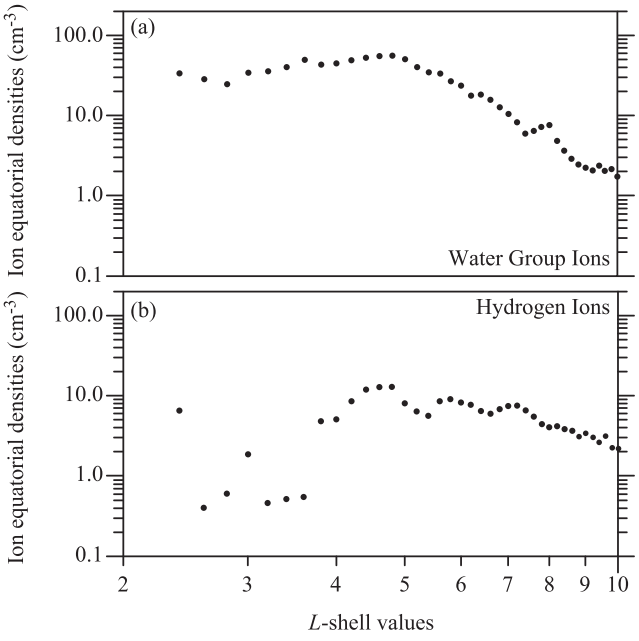

Figure 7. A plot of the equatorial densities for the water group ions (panel a) and hydrogen ions (panel b), obtained from the best fit of the diffusive equilibrium density model to the measured electron densities. The densities of both ion species exhibit density peaks at $L = 2.4$ in the extended ring ionosphere and broad density peaks just beyond the orbit of Enceladus. Smaller ion density peaks are observed at $L = 5.8$ and $L = 7.0$.

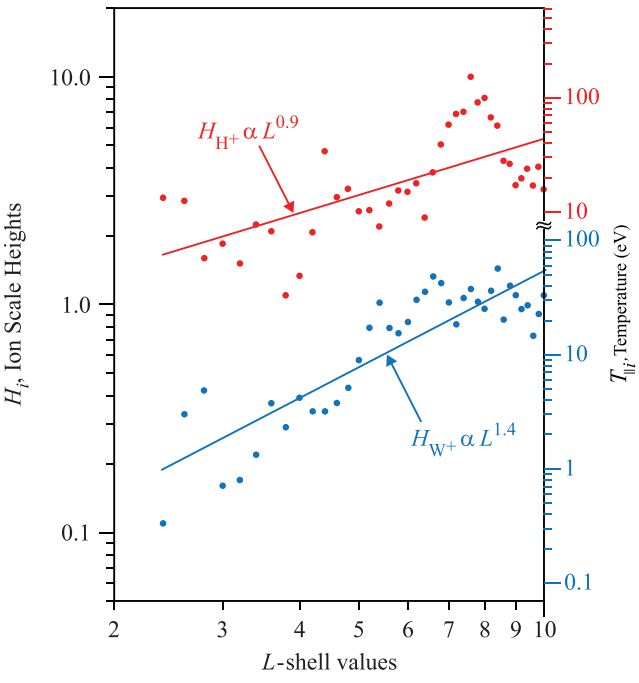

Figure 8. A plot of the ion scale heights for the water group ions (in blue) and the hydrogen ions (in red) derived from the best fit of the diffusive equilibrium density model to the measured electron densities. The scale heights for both species increase with increasing L value. The best fit lines through the scale height distributions show an L-shell dependence of 1.4 for the water group ions and 0.9 for the hydrogen ions.

hydrogen ions. The dominant water group ions constrain the fit at the lower latitude end of the density distribution and the hydrogen ions constrain the fit at the higher latitude end.

Figure 6a shows the local minimum (white circle) in chi-square for the water group ion equatorial density (vertical axis) as a function of the scale height (horizontal axis). Figure 6b shows the local minimum in chi-square for the hydrogen ion equatorial density and the scale height. The white circles in these two upper panels represent the best fit solution of the density model to the measured electron densities in panel c. These circles are bounded by dark regions, the local minimum in chi-square that is represented by the color bar. The model fit shown in Figure 6c is a good fit to the data. For this $L = 3.4$ bin, the model fit to the measured electron densities gives $n_{eqW^+} = 40.18\,\mathrm{cm}^{-3}$, $n_{eqH^+} = 0.52\,\mathrm{cm}^{-3}$, $H_{W^+} = 0.22$, and $H_{H^+} = 2.25$. These ion parameters as well as the electron temperature (W_e) and the ion anisotropies (A_{W^+} and A_{H^+}), are listed in the upper corner of panel c in Figure 6.

In addition to the equatorial ion densities and ion scale heights that are derived from the diffusive equilibrium density model, the electrostatic potential is numerically solved at each point along the magnetic field line, using the charge neutrality condition, $n_e = n_{W^+} + n_{H^+}$, and equation 4. Figure 6d is a plot of the electrostatic potential along the $L = 3.4$ field line from equatorial latitudes to $\lambda = 35°$, the highest latitude evaluated in the diffusive equilibrium model. Values for the electrostatic potential along each of the 39 field lines in this density model are listed in Table S1 in the supporting information.

The diffusive equilibrium model is fit to the averaged RPWS electron density measurements in 0.2 R_S increments over the $2.4 \leq L \leq 10$ range of L-shell values. Each of these 39 model fits yields best values for the ion equatorial densities and the ion scale heights, which are listed in Table 2. In this table, the L-shell in the first column represents the center of each 0.4 R_S averaging bin. The distribution of the equatorial densities with distance from Saturn is shown in Figure 7 for the water group ions (panel a) and the hydrogen ions (panel b). The modeled W^+ ion densities are comparable to the CAPS densities over the same L-shell range, but the modeled H^+ ion densities are roughly two times higher than the CAPS H^+ densities (Wilson et al., 2017). The density of both ion species peaks at ~2.4 R_S in agreement with electron density measurements in the extended ring ionosphere (Gurnett et al., 2005; Persoon et al., 2015) and at ~4.5 R_S, in agreement with the Enceladus electron density peak (Livi et al., 2014; Persoon et al., 2009, 2013). The weak density peaks in the H^+ density profile centered on $L = 5.8$ and $L = 7.0$, just beyond the orbits of Tethys and Dione, are also observed in the earlier diffusive equilibrium model of the H^+ densities at $L = 7$ (Persoon et al., 2009) and in the RPWS/LP ion density measurements at the orbit of Tethys (Holmberg et al., 2012). The weak density peaks occur in the same magnetospheric region as the broad peak in the total ion flux tube content, calculated from CAPS measurements, near Dione's L-shell at ~6.3 R_S (Sittler et al., 2008). Pioneer density measurements of the oxygen ions showed strong density peaks at the orbits of both moons (Frank et al., 1980). Burch et al. (2007) suggest that plasma sources may be associated with Tethys and Dione, possibly by sputtering off the moons' icy surfaces. Evidence for a sputtering-induced atmosphere at Dione is presented by Simon et al. (2011) and Teolis and Waite (2016).

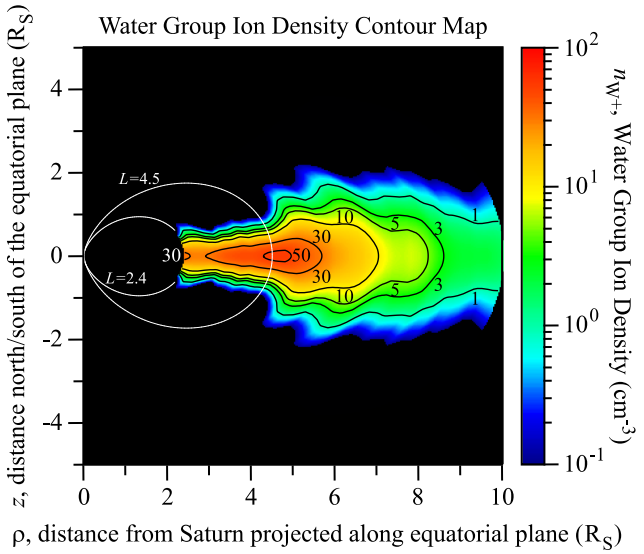

Figure 9. A meridional density contour plot for the water group ions constructed from the diffusive equilibrium model for Saturn's inner magnetosphere. The contour plot assumes mirror symmetry about the equatorial plane and azimuthal symmetry about Saturn's spin axis. The contour plot for the water group ions shows a density peak exceeding 30 cm^{-3} in the extended ring atmosphere and a broad density peak exceeding 50 cm^{-3} just beyond the Enceladus orbit at $L = 4$.

Figure 8 shows the ion scale heights derived from the diffusive equilibrium model fit to the RPWS electron density measurements. Although they are highly variable, the ion scale heights for both species expand with increasing L value. Consistent with the confinement of the heavier ions near the equatorial plane, the scale height for the water group ions is a half order of magnitude lower than the hydrogen ion scale height at higher L-shell values, increasing to an order of magnitude lower than the hydrogen ion scale height at $L = 2.4$, and shows a similar radial dependence to the water group ion scale heights in Thomsen et al. (2010) and Wilson et al. (2017) over corresponding L-shell ranges. The water group ion scale heights vary from $H_{W^+} = 0.11$ at $L = 2.4$ to $H_{W^+} = 1.1$ at $L = 10$. The hydrogen ion scale heights vary from $H_{H^+} = 2.95$ at $L = 2.4$ to $H_{H^+} = 3.21$ at $L = 10$. The best fit lines through the ion scale height distributions over the range of L-shell values show an L-shell dependence of 1.4 for the water group ions, similar to the results in the earlier density model derived from the magnetic field-aligned force equation (Persoon et al., 2009). The hydrogen ion scale heights are highly variable and show an L-shell dependence of 0.9, lower than the L-shell dependence of 1.4 in the earlier model for $L \geq 3.6$(Persoon et al., 2009).

Since the dimensionless scale height is a function of the ion temperature (Persoon et al., 2009), the color-coded ion temperatures corresponding to the water group and hydrogen ion scale heights are displayed on the right vertical axis in Figure 8. The best fit for the water group ion temperatures (blue line) ranges from 0.4 to 80 eV over the range of L-shell values and for the hydrogen ion temperatures (red line) from 5 to 45 eV. At $L = 10$ R_S, both of the ion temperatures are similar, as expected. Although there is considerable scatter in the ion temperatures, the range of water group ion temperatures is consistent with the CAPS water group ion temperatures in Wilson et al. (2008) but varies from the CAPS ion temperatures in Thomsen et al. (2010) and Wilson et al. (2017) by ±50% over a comparable range of L-shell values. The range of hydrogen ion temperatures is a factor of two higher than the CAPS hydrogen ion temperatures (Thomsen et al., 2010; Wilson et al., 2008, 2017).

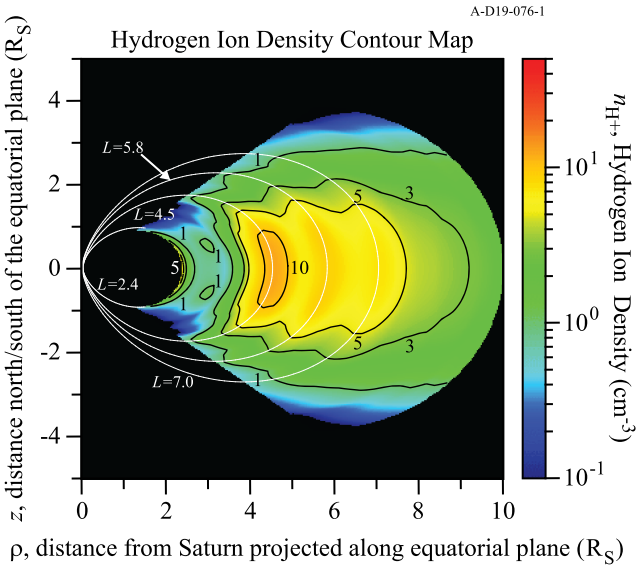

Figure 10. A meridional density contour plot for the hydrogen ions constructed from the diffusive equilibrium model for Saturn's inner magnetosphere. The contour plot illustrates the expansion of the hydrogen ions away from the equatorial plane under the influence of a strong ambipolar force with a strong density peak exceeding 5 cm^{-3} in the extended ring atmosphere and a strong density peak exceeding 10 cm^{-3} just beyond the Enceladus orbit at $L = 4$. Smaller ion density peaks and weaker plasma expansion are observed at $L = 5.8$ and $L = 7.0$.

The process of fitting the diffusive equilibrium model to the electron density measurements, demonstrated in Figure 6, illustrates the strengths and the difficulties in deriving the four plasma parameters shown in Figures 7 and 8. In Figure 6a, the dark oval region defines the local minimum for the data fit. Both the equatorial density and the scale height for the water group ions are well constrained within this oval. In Figure 6b, the equatorial density for the hydrogen ions is constrained inside the dark blue region. However, the hydrogen scale height is not well constrained. The best fit of the model for the other three plasma parameters is used to constrain the range of the H^+ scale height parameter. These features in the model fit are typical of most of the 39 averaging bins. The equatorial densities and scale heights for the water group ions are well constrained inside $L = 9$. These two parameters are poorly constrained for $L \geq 9$. This is attributed to the sparsely populated density bins at higher L-shells. Fewer available density measurements at higher latitudes result in H^+ equatorial densities that are not as well constrained inside $L = 4$ and contribute to the wide scatter in the H^+ equatorial densities at lower L-shells in Figure 7b. The hydrogen scale height is not well constrained for the majority of the averaging bins. This is evidenced by the wide scatter and lower L-shell dependence of the H^+ scale heights in Figure 8.

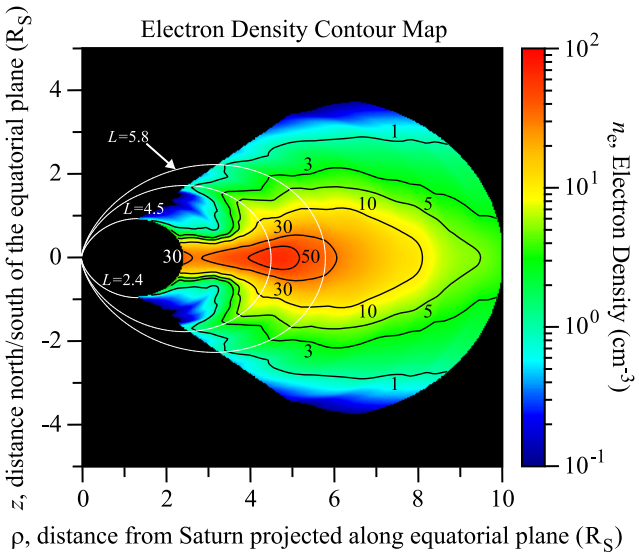

Figure 11. A meridional density contour plot for the electrons constructed from the diffusive equilibrium model for Saturn's inner magnetosphere. As in the water group ion density contour plot in Figure 9, the electron distribution shows similar density peaks near the equatorial plane at $L = 2.4$ and just beyond $L = 4$. A comparison with the hydrogen ion density contour plot in Figure 10 shows a similar expansion of the electrons along field lines connecting to these peak density regions.

6. Density Contour Plots

Meridional density contour plots have been constructed for the two ion species and the electrons to illustrate the plasma distribution in Saturn's inner magnetosphere. These contour plots are created assuming mirror symmetry about the equatorial plane and azimuthal symmetry about Saturn's spin axis. A three-point sliding average was used to create smoother representations of the ion equatorial densities (n_{eqi}) and the ion scale heights (H_i) in Figures 7 and 8 as functions of the L-value. These smoothed values are then used in the model fit to iteratively solve for the electrostatic potential (Φ) as a function of L for each L-shell bin. The electrostatic potentials are listed in Table S1 in the supporting information. By inserting electron temperatures and ion anisotropies from Table 1 and making the appropriate substitutions for latitude (λ) and L value, all of the variables are now available to solve equations 2, 3, and 4 and to compute the plasma density at any point (ρ, z) in the meridian plane.

The density contours for the water group ions in the meridian plane are shown in Figure 9. The contour map clearly supports the accepted hypothesis that Enceladus is the primary plasma source in Saturn's inner magnetosphere. The water group ion density exceeds 50 cm^{-3} between $L = 4$ and $L = 5$, consistent with the electron density measurements, which track the dominant water group ion densities near the equator and peak at 70 cm^{-3} at ~4.5 R_S (Persoon et al., 2009, 2013). The addition of data from the ring-grazing orbits made it possible to extend the density model inward to $L = 2.4$ and identify a second plasma source, the extended ring atmosphere. A second water group ion density peak, where the ion density exceeds 30 cm^{-3}, occurs at $L = 2.4$, where the averaged electron density measurements obtained during SOI and the ring-grazing orbits are in excess of 30 cm^{-3}. Consistent with earlier observations (Sittler et al., 2008; Thomsen et al., 2010; Young et al., 2005), the dominant water group ions are centrifugally confined within 1–2 Saturn radii of the equatorial plane in Saturn's inner magnetosphere.

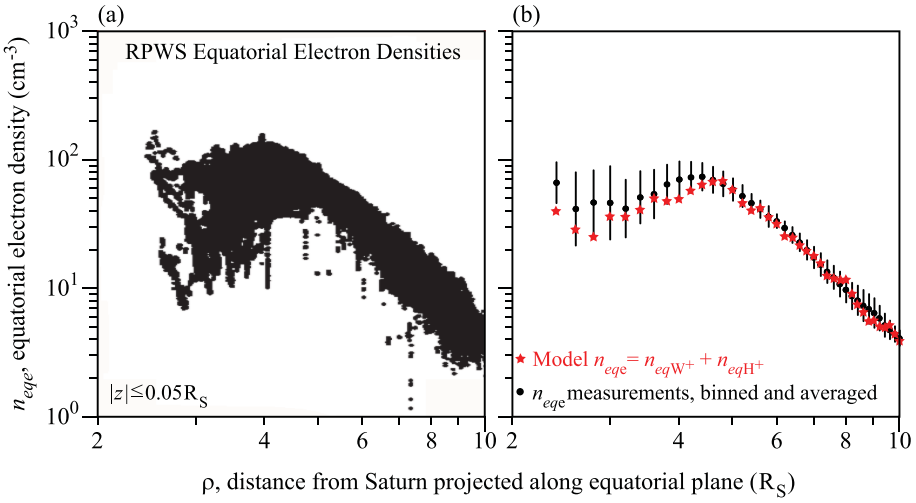

Figure 12. A comparison of the modeled equatorial electron densities and the measured electron densities. Panel a shows the RPWS and RPWS/LP electron density measurements within 0.05 R_S of the equatorial plane from 30 June 2004 until 19 April 2017. Panel b shows these density measurements averaged in L-shell bins of 0.4 R_S and smoothed with a sliding average in increments of 0.2 R_S (black circles). The error bars represent one standard deviation of the averaged densities. The modeled electron densities for the same averaging bins (red stars) have been derived from the charge neutrality condition using the ion equatorial densities obtained from the fit of the diffusive equilibrium density model (Table 2).

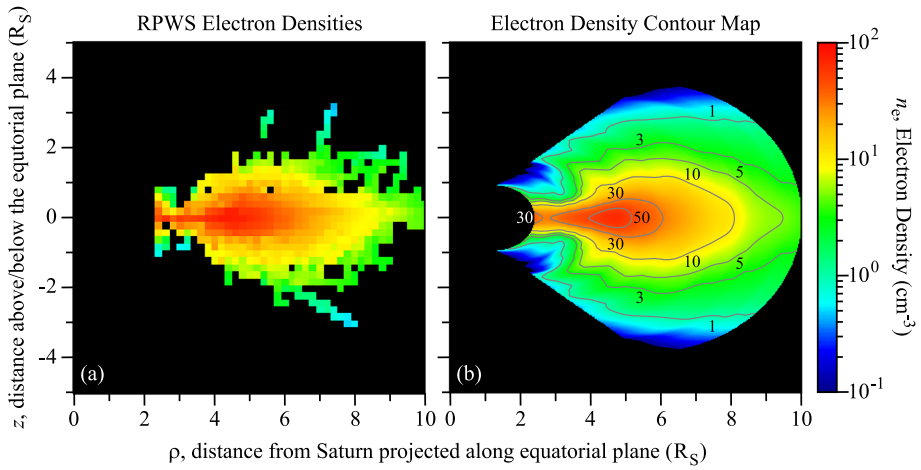

Figure 13. Meridional plot of the measured RPWS and RPWS/LP electron density measurements (panel a) and the meridional contour map of the electron densities from the diffusive equilibrium model (panel b), also shown in Figure 11. Both plots show equatorial density peaks at $L = 2.4$ and in the region surrounding Enceladus. And both plots show plasma expansion along the field lines mapping to the Janus/Epimetheus ring, although the modeled densities tend to be up to a half order of magnitude lower than the measured densities at higher latitudes.

The density contours for the hydrogen ions are shown in Figure 10. As in earlier density models (Persoon et al., 2009; Sittler et al., 2008), these lighter ions are clearly expanding along the field lines away from the equatorial plane under the influence of a strong ambipolar force, with a stronger plasma expansion along field lines associated with the density peak of the Enceladus plasma between $L = 4$ and $L = 5$. This density model is the first to show a strong expansion of the light hydrogen ions and the electrons (in the next figure) along the $L = 2.4$ and adjacent field lines that connect to the plasma density peak in the extended ring ionosphere observed in Figure 9. A weaker light ion density peak can be seen centered at ~$L = 5.8$ between the orbits of Tethys ($L = 4.9$) and Dione ($L = 6.3$) and at ~L=7 with a weaker expansion along connecting field lines, consistent with the hydrogen ion density peaks in Figure 7.

The features observed in the ion density contour plots are also seen in the electron density contour map in Figure 11. There is a strong peak in the electron density associated with the Enceladus source where the electron density exceeds 50 cm^{-3} and a strong but secondary peak in the electron density associated with the plasma source in the extended ring atmosphere where the electron density exceeds 30 cm^{-3}. There is also strong and consistent evidence for electron expansion along field lines connecting to these peak density regions. Evidence for weaker electron expansion to higher latitudes at $L = 5.8$ between the orbits of Tethys and Dione is similar to the weak expansion of the light ions along the same field lines in Figure 10.

Complete tables of all (n, ρ, and z) data points that were used to construct the density contour maps in Figures 9–11 are available in the Zenodo website (https://zenodo.org/10.5281/zenodo.3583302).

7. Electron Density Measurements and the Diffusive Equilibrium Model

Meridional density contour plots for ions and electrons have been constructed from plasma parameters that have been smoothed through binning and sliding averages to illustrate the trends in the magnetospheric plasma distribution. At this point, we can look at how the modeled plasma distribution compares with the measured electron densities. Figure 12 compares the measured and modeled equatorial electron densities. Panel a shows the radial dependence of the RPWS and LP electron density measurements within 0.05 R_S of the equatorial plane over an L-shell range of $2.4 \leq L \leq 10.0$ from 30 June 2004 until 19 April 2017. The outward diffusion of the electrons under a strong centrifugal force is evident beyond 5 R_S. But inside 5 R_S, the highly variable density measurements are a mixture of plasma diffusing inward from the Enceladus source and plasma diffusing outward from the extended ring atmosphere. These density measurements have been averaged in L-shell bins of 0.4 R_S (the black circles in panel b) and smoothed with a sliding average in increments of 0.2 R_S. The error bars in this figure represent one standard deviation of the averaged densities.

The modeled equatorial electron densities in panel b have been derived from the charge neutrality condition using the ion equatorial densities in Table 2 and plotted as red stars for the same L-shell bins. These modeled electron densities closely track the averaged density measurements beyond 5 R_S and remain within the error bars inside 5 R_S. The modeled densities inside 5 R_S can be increased with substantial increases in the ion anisotropies, but these increases cannot be reasonably validated with any currently existing data.

Figure 13 compares the distribution of the measured and modeled electrons in the inner magnetosphere. Panel a provides a meridional view of all of the RPWS electron density measurements averaged in 0.2 R_S bins in (ρ, z) space. The electron densities are color coded using the same color bar as the electron density contour map (from Figure 11) in panel b. Beyond $L = 4$, the modeled densities correlate well with the density measurements. But as noted in the right panel of Figure 12, the modeled electron densities, especially inside 3 R_S, tend to be lower than the measured densities. Both plots show equatorial density peaks at $L = 2.4$ and in the region surrounding Enceladus at $L = 4$ and both plots show plasma expansion along the field lines mapping to the Janus/Epimetheus ring. However, the modeled densities tend to be up to a half order of magnitude lower than the measured densities at higher latitudes inside $L = 3$. The map of the RPWS measured electron densities shows a strong signature for plasma expansion to higher latitudes along field lines mapping to the extended ring atmosphere at 2.4 R_S just beyond the outer boundary of the main rings.

8. Summary

The diffusive equilibrium density model maps the distribution of the thermal plasma in Saturn's inner magnetosphere. The density contour maps are derived from model fits to electron densities that have been summed over solar cycle and seasonal variations of the plasma inside the Enceladus orbit (Elrod et al., 2012, 2014; Persoon et al., 2015), local time variations (Morooka et al., 2009) and longitudinal variations both inside 5 R_S (Gurnett et al., 2007) and beyond 7 R_S (Morooka et al., 2009). For the plasma beyond the Enceladus orbit, the electron densities have been summed and averaged over 13 years of the Cassini mission, minimizing these density variations and providing a map of the general trend in the plasma distribution. However, at lower L-shells, many of the electron density measurements were obtained from a more limited number of orbits over a narrower range of time and latitude (see Figure 1). Most importantly, the ring-grazing orbits provided the densities for the lowest L-shell bins in this study. These density measurements were obtained between November 2016 and April 2017, as Saturn was approaching the northern summer solstice when the electron densities at the lowest L-shells are expected to peak (Persoon et al., 2015).

There are several simplifying assumptions used in deriving the diffusive equilibrium model. The electron temperatures, assumed to be constant along the field lines, are known to have day/night asymmetries (Thomsen et al., 2012), as well as latitudinal variations (Gustafsson & Wahlund, 2010). The ion anisotropies are derived from equatorial ion parameters and are also assumed to be constant with latitude. At this point, there is not enough data to confirm this assumption. The larger problem with the ion anisotropies is the uncertainty in the region inside $L = 5$, where pickup ions and penetrating background radiation can result in elevated anisotropies, and the lack of any CAPS measurements during the final year of the mission when Cassini explored Saturn's magnetosphere just beyond the main rings.

The most problematic of the simplifying assumptions for the diffusive equilibrium model is the central assumption of charge neutrality. Strong dust-plasma coupling exists throughout the E ring but significantly voids the charge neutrality condition in the vicinity of the Enceladus plume at 3.95 R_S (Morooka et al., 2011) and in the vicinity of the Janus/Epimetheus ring at ~2.5 R_S (Morooka et al., 2018). There are few RPWS electron density measurements available inside the Enceladus plume region, because dust impacts on the electric antennas obscure the upper hybrid resonance emissions from which the electron densities are derived. However, the ring-grazing orbits carried Cassini through the dusty Janus/Epimetheus rings. At equatorial latitudes, large differences between the electron and ion densities were attributed to electron absorption by the dust particles (Morooka et al., 2018). A future diffusive equilibrium density model might include an adjustment to the charge neutrality condition in the dense dusty regions.

The diffusive equilibrium density model provides a valuable global map of the plasma distribution in Saturn's inner magnetosphere and hints at plasma processes requiring further study. The small but significant H^+ density increases in the Tethys/Dione region suggest that additional plasma may be created in this

region. The model provides stronger evidence for the expansion of plasma along the magnetic field lines that map to the extended ring atmosphere and to the region just beyond the Enceladus orbit where the Enceladus plasma density peaks. In the extended ring ionosphere, the elevated densities at higher latitudes could also indicate that plasma is moving into this region from a third plasma source in Saturn's ionosphere.

Acknowledgments
The Cassini radio and plasma wave research at the University of Iowa is supported by NASA through JPL contract 1415150. The Langmuir Probe research at the Swedish Institute of Physics was supported by the Swedish National Space Board under contract Dnr 174/15. The derivation of CAPS anisotropies provided by R. J. Wilson was funded by JPL/NASA under contract 1405851. The RPWS electron density data are available at Planetary Data System (https://doi.org/10.17189/1518302). The QTN electron temperature data are available at Planetary Data System (https://doi.org/10.17189/1518376) and online (http://www.lesia.obspm.fr/kronos/data/qtn/data/). The RPWS/LP electron density and electron temperature data used in this study are available at Planetary Data System (Wahlund, J.-E., W.S. Kurth, and L.J. Granroth CASSINI SS/S RPWS DERIVED LANGMUIR PROBE SWEEP V1.0, CO-SS/S-RPWS-5-LPSWEEP-V1.0, NASA Planetary Data System, 2018) (https://pds-ppi.igpp.ucla.edu/data/CO-SS_S-RPWS-5-LPSWEEP-V1.0/DATA/SATURN/).

References

Bridge, H. S., Bagenal, F., Belcher, J. W., Lazarus, A. J., McNutt, R. L., Sullivan, J. D., et al. (1982). Plasma observations near Saturn: Initial results from Voyager 2. *Science*, *215*(4532), 563–570. https://doi.org/10.1126/science,215.4532.563

Bridge, H. S., Belcher, J. W., Lazarus, A. J., Olbert, S., Sullivan, J. D., Bagenal, F., et al. (1981). Plasma observations near Saturn: Initial results from Voyager 1. *Science*, *212*(4491), 217–224. https://doi.org/10.1126/science.212.4491.217

Burch, J. L., Goldstein, J., Lewis, W. S., Young, D. T., Coates, A. J., Dougherty, M. K., & Andre, N. (2007). Tethys and Dione as sources of outward-flowing plasma in Saturn's magnetosphere. *Nature*, *447*. https://doi.org/10.1038/nature05906

Coates, A. J., McAndrews, H. J., Rymer, A. M., Young, D. T., Crary, F. J., Maurice, S., et al. (2005). Plasma electrons above Saturn's main rings: CAPS observations. *Geophysical Research Letters*, *32*, L14S09. https://doi.org/10.1029/2005GL022694

Elrod, M. K., Tseng, W.-L., Wilson, R. J., & Johnson, R. E. (2012). Seasonal variations in Saturn's plasma between the main rings and Enceladus. *Journal of Geophysical Research*, *117*, A03207. https://doi.org/10.1029/2011JA017332

Elrod, M. K., Tseng, W.-L., Woodson, A. K., & Johnson, R. E. (2014). Seasonal and radial trends in Saturn's thermal plasma between the main rings and Enceladus. *Icarus*, *242*, 130–137. https://doi.org/10.1016/j.icarus.2014.07.020

Eviatar, A., McNutt, R. L., Siscoe, G. L., & Sullivan, J. D. (1983). Heavy ions in the outer Kronian magnetosphere. *Journal of Geophysical Research*, *88*, 823–831.

Farrell, W. M., Kurth, W. S., Gurnett, D. A., Johnson, R. E., Kaiser, M. L., Wahlund, J.-E., & Waite, J. H. (2009). Electron density dropout near Enceladus in the context of water-vapor and water-ice. *Geophysical Research Letters*, *36*, L10203. https://doi.org/10.1029/2008GL037108

Frank, L. A., Burek, B. G., Ackerson, K. L., Wolfe, J. H., & Mihalov, J. D. (1980). Plasmas in Saturn's magnetosphere. *Journal of Geophysical Research*, *85*. https://doi.org/10.1029/JA085iA11p05695

Gurnett, D. A., Kurth, W. S., Hospodarsky, G. B., Persoon, A. M., Averkamp, T. F., Cecconi, B., et al. (2005). Radio and plasma wave observations at Saturn from Cassini's approach and first orbit. *Science*, *307*(5713), 1255–1259. https://doi.org/10.1126/science.1105356

Gurnett, D. A., Kurth, W. S., Kirchner, D. L., Hospodarsky, G. B., Averkamp, T. F., Zarka, P., et al. (2004). The Cassini radio and plasma wave investigation. In C. T. Russell (Ed.), *The Cassini-Huygens Mission* (Vol. *2*, pp. 395–463). Dordrecht, The Netherlands: Kluwer Academic Publishers. https://doi.org/10.1007/978-1-4020-2774-1_6

Gurnett, D. A., Persoon, A. M., Kurth, W. S., Groene, J. B., Averkamp, T. F., Dougherty, M. K., & Southwood, D. J. (2007). The variable rotation period of the inner region of Saturn's plasma disk. *Science*, *316*. https://doi.org/10.1126/science.1138562

Gustafsson, G., & Wahlund, J.-E. (2010). Electron temperatures in Saturn's plasma disc. *Planetary and Space Science*, *58*. https://doi.org/10.1016/j.pss.2010.03.007

Holmberg, M. K. G., Wahlund, J.-E., Morooka, M. W., & Persoon, A. M. (2012). Ion densities and velocities in the inner plasma torus of Saturn. *Planetary and Space Science*, *73*(1), 151–160. https://doi.org/10.1016/j.pss.2012.09.016

Ip, W.-H. (2005). An update on the ring exosphere and plasma disc of Saturn. *Geophysical Research Letters*, *32*, L13204. https://doi.org/10.1029/2004GL022217

Johnson, R. E., Luhmann, J. G., Tokar, R. L., Bouhram, M., Berthelier, J. J., Sittler, E. C., et al. (2006). Production, ionization and redistribution of O_2 in Saturn's ring atmosphere. *Icarus*, *180*(2), 393–402. https://doi.org/10.1016/j.icarus.2005.08.021

Johnson, R. E., Tseng, W.-L., Elrod, M. K., & Persoon, A. M. (2017). Nanograin density outside Saturn's A ring. *Astronomical Journal Letters*, *834*(1), L6. https://doi.org/10.3847/2041-8213/834/1/L6

Jurac, S., McGrath, M. A., Johnson, R. E., Richardson, J. D., Vasyliunas, V. M., & Eviatar, A. (2002). Saturn: Search for a missing water source. *Geophysical Research Letters*, *29*(24), 2172. https://doi.org/10.1029/2002GL015855

Jurac, S., & Richardson, J. D. (2005). A self-consistent model of plasma and neutrals at Saturn: Neutral cloud morphology. *Journal of Geophysical Research*, *110*, A09220. https://doi.org/10.1029/2004JA010635

Lazarus, A. J., & McNutt, R. L. (1983). Low-energy plasma ion observations in Saturn's magnetosphere. *Journal of Geophysical Research*, *88*, 8831–8846. https://doi.org/10.1029/JA088iA11p08847

Leisner, J. S., Russell, C. T., Dougherty, M. K., Blanco-Cano, X., Strangeway, R. J., & Bertucci, C. (2006). Ion cyclotron waves in Saturn's E ring: Initial Cassini observations. *Geophysical Research Letters*, *33*, L11101. https://doi.org/10.1029/2005GL024875

Livi, R., Goldstein, J., Burch, J. L., Crary, F., Rymer, A. M., Mitchell, D. G., & Persoon, A. M. (2014). Multi-instrument analysis of plasma parameters in Saturn's equatorial, inner magnetosphere using corrections for spacecraft potential and penetrating background radiation. *Journal of Geophysical Research: Space Physics*, *119*, 3683–3707. https://doi.org/10.1002/2013JA019616

Maurice, S., Blanc, M., Prange, R., & Sittler, E. C. (1997). The magnetic field-aligned polarization electric field and its effects on particle distribution in the magnetospheres of Jupiter and Saturn. *Planetary and Space Science*, *45*, 1449–1465.

Maurice, S., Sittler, E. C., Cooper, J. F., Mauk, B. H., Blanc, M., & Selesnick, R. S. (1996). Comprehensive analysis of electron observations at Saturn: Voyager 1 and 2. *Journal of Geophysical Research*, *101*(A7), 15,211–15,232. https://doi.org/10.1029/96JA00765

Moncuquet, M., Lecacheux, A., Meyer-Vernet, N., Cecconi, B., & Kurth, W. S. (2005). Quasi-thermal noise spectroscopy in the inner magnetosphere of Saturn with Cassini/RPWS: Electron temperatures and density. *Geophysical Research Letters*, *32*, L20S02. https://doi.org/10.1029/2005GL022508

Morooka, M. W., Modolo, R., Wahlund, J.-E., Andre, M., Eriksson, A. I., Persoon, A. M., et al. (2009). The electron density of Saturn's magnetosphere. *Annales Geophysicae*, *27*(7), 2971–2991. https://doi.org/10.5194/angeo-27-2971-2009

Morooka, M. W., Wahlund, J.-E., Andrews, D. J., Persoon, A. M., Ye, S.-Y., Kurth, W. S., et al. (2018). The dusty plasma disk around the Janus/Epimetheus Ring. *Journal of Geophysical Research: Space Physics*, *123*, 4668–4678. https://doi.org/10.1002/2017JA024917

Morooka, M. W., Wahlund, J.-E., Eriksson, A. I., Farrell, W. M., Gurnett, D. A., Kurth, W. S., et al. (2011). Dusty plasma in the vicinity of Enceladus. *Journal of Geophysical Research*, *116*, A12221. https://doi.org/10.1029/2011JA017038

Morooka, M. W., Wahlund, J.-E., Hadid, L. Z., Eriksson, A. J., Edberg, N. J. T., Vigren, E., et al. (2019). Saturn's dusty ionosphere. *Journal of Geophysical Research: Space Physics*, *124*, 1679–1697. https://doi.org/10.1029/2018JA926154

Persoon, A. M., Gurnett, D. A., Kurth, W. S., & Groene, J. B. (2006). A simple scale height model of the electron density in Saturn's plasma disk. *Geophysical Research Letters*, *33*, L18106. https://doi.org/10.1029/2006GL027090

Persoon, A. M., Gurnett, D. A., Kurth, W. S., Groene, J. B., & Faden, J. B. (2015). Evidence for a seasonally dependent ring plasma in the region between Saturn's A ring and Enceladus' orbit. *Journal of Geophysical Research: Space Physics*, *120*, 6276–6285. https://doi.org/10.1002/2015JA021180

Persoon, A. M., Gurnett, D. A., Kurth, W. S., Hospodarsky, G. B., Groene, J. B., Canu, P., & Dougherty, M. K. (2005). Equatorial electron density measurements in Saturn's inner magnetosphere. *Geophysical Research Letters*, *32*, L23105. https://doi.org/10.1029/2005GL024294

Persoon, A. M., Gurnett, D. A., Leisner, J. S., Kurth, W. S., Groene, J. B., & Faden, J. B. (2013). The plasma density distribution in the inner region of Saturn's magnetosphere. *Journal of Geophysical Research: Space Physics*, *118*, 2970–2974. https://doi.org/10.1002/jgra.50182

Persoon, A. M., Gurnett, D. A., Santolik, O., Kurth, W. S., Faden, J. B., Groene, J. B., et al. (2009). A diffusive equilibrium model for the plasma density in Saturn's magnetosphere. *Journal of Geophysical Research*, *114*, A04211. https://doi.org/10.1029/2008JA013912

Richardson, J. D. (1986). Thermal ions at Saturn: Plasma parameters and implications. *Journal of Geophysical Research*, *91*, 1381–1389.

Richardson, J. D. (1995). An extended plasma model for Saturn. *Geophysical Research Letters*, *22*, 1177–1180. https://doi.org/10.1029/95GL01018

Richardson, J. D. (1998). Thermal plasma and neutral gas in Saturn's magnetosphere. *Reviews of Geophysics*, *36*, 501–524. https://doi.org/10.1029/98RG01691

Richardson, J. D., Eviatar, A., McGrath, M. A., & Vasyliunas, V. M. (1998). OH in Saturn's magnetosphere: Observations and implications. *Journal of Geophysical Research*, *103*, 20,245–20,255.

Richardson, J. D., & Jurac, S. (2004). A self-consistent model of plasma and neutrals at Saturn: The ion tori. *Geophysical Research Letters*, *31*, L24803. https://doi.org/10.1029/2004GL020959

Richardson, J. D., & Sittler, E. C. (1990). A plasma density model for Saturn based on Voyager observations. *Journal of Geophysical Research*, *95*(A8), 12019. https://doi.org/10.1029/JA095iA08p12019

Schippers, P., Blanc, M., Andre, N., Dandouras, I., Lewis, G. R., Gilbert, L. K., et al. (2008). Multi-instrument analysis of electron populations in Saturn's magnetosphere. *Journal of Geophysical Research*, *113*, A07208. https://doi.org/10.1029/2008JA013098

Schippers, P., Moncuquet, M., Meyer-Vernet, N., & Lecacheux, A. (2013). Core electron temperature and density in the innermost Saturn's magnetosphere from HF power spectra analysis on Cassini. *Journal of Geophysical Research: Space Physics*, *118*, 7170–7180. https://doi.org/10.1002/2013JA019199

Simon, S., Saur, J., Neubauer, F. M., Wennmacher, A., & Dougherty, M. K. (2011). Magnetic signatures of a tenuous atmosphere at Dione. *Geophysical Research Letters*, *38*, LL15102. https://doi.org/10.1029/2011GL0484454

Sittler, E. C., Andre, N., Blanc, M., Burger, M., Johnson, R. E., Coates, A. J., et al. (2008). Ion and neutral sources and sinks within Saturn's inner magnetosphere: Cassini results. *Planetary and Space Science*, *56*(1), 3–18. https://doi.org/10.1016/j.pss.2007.06.006

Sittler, E. C., Ogilvie, K. W., & Scudder, J. D. (1983). Survey of low-energy plasma electrons in Saturn's magnetosphere: Voyagers 1 and 2. *Journal of Geophysical Research*, *88*(A11), 8847–8870. https://doi.org/10.1029/JA088iA11p08847

Teolis, B. D., & Waite, J. H. (2016). Dione and Rhea seasonal exospheres revealed by Cassini CAPS. *Icarus*, *272*, 277–289. https://doi.org/10.1016/j.icarus.2016.02.031

Thomsen, M. F., Reisenfeld, D. B., DeLapp, D. M., Tokar, R. L., Young, D. T., Crary, F. J., et al. (2010). Survey of ion plasma parameters in Saturn's magnetosphere. *Journal of Geophysical Research*, *115*, A10220. https://doi.org/10.1029/2010JA015267

Thomsen, M. F., Roussos, E., Andriopoulou, M., Kollman, P., Arridge, C. S., Paranicas, C. P., et al. (2012). Saturn's inner magnetospheric convection pattern: Further evidence. *Journal of Geophysical Research*, *117*, A09208. https://doi.org/10.1029/2011JA017482

Tokar, R. L., Wilson, R. J., Johnson, R. E., Henderson, M. G., Thomsen, M. F., Cowee, M. M., et al. (2008). Cassini detection of water-group pick-up ions in the Enceladus torus. *Geophysical Research Letters*, *35*, L14202. https://doi.org/10.1029/2008GL034749

Trainor, J. H., McDonald, F. B., & Schardt, A. W. (1980). Observations of energetic ions and electrons in Saturn's magnetosphere. *Science*, *207*(4429), 421–425. https://doi.org/10.1126/science.207.4429.421

Wahlund, J.-E., Bostrom, R., Gustafsson, G., Gurnett, D. A., Kurth, W. S., Averkamp, T., et al. (2005). The inner magnetosphere of Saturn: Cassini RPWS cold plasma results from the first encounter. *Geophysical Research Letters*, *32*, L20S09. https://doi.org/10.1029/2005GL022699

Wilson, R. J., Bagenal, F., & Persoon, A. M. (2017). Survey of thermal plasma ions in Saturn's magnetosphere utilizing a forward model. *Journal of Geophysical Research: Space Physics*, *122*, 7256–7278. https://doi.org/10.1002/2017JA024117

Wilson, R. J., Tokar, R. L., Henderson, M. G., Hill, T. W., Thomsen, M. F., & Pontius, D. H. (2008). Cassini plasma spectrometer thermal ion measurements in Saturn's inner magnetosphere. *Journal of Geophysical Research*, *113*, A12218. https://doi.org/10.1029/2008JA013486

Wolfe, J. H., Mihalov, J. D., Collard, H. R., McKibbin, D. D., Frank, L. A., & Intriligator, D. S. (1980). Preliminary results on the plasma environment of Saturn from the Pioneer 11 Plasma Analyzer Experiment. *Science*, *207*. https://doi.org/10.1126/science.207.4429.403

Ye, S.-Y., Gurnett, D. A., Kurth, W. S., Averkamp, T. F., Morooka, M., Sakai, S., & Wahlund, J.-E. (2014). Electron density inside Enceladus plume inferred from plasma oscillations excited by dust impacts. *Journal of Geophysical Research: Space Physics*, *119*, 3373–3380. https://doi.org/10.1002/2014JA019861

Young, D. T., Berthelier, J.-J., Blanc, M., Burch, J. L., Bolton, S., Coates, A. J., et al. (2005). Composition and dynamics of plasma in Saturn's magnetosphere. *Science*, *307*(5713), 1262–1266. https://doi.org/10.1126/science.1106151

Young, D. T., Berthelier, J. J., Blanc, M., Burch, J. L., Coates, A. J., Goldstein, R., et al. (2004). Cassini plasma spectrometer investigation. In C. T. Russell (Ed.), *The Cassini-Huygens Mission* (Vol. *2*, pp. 1–112). Dordrecht, The Netherlands: Kluwer Academic Publishers. https://doi.org/10.1007/978-1-4020-2774-1_1